ADVANCES IN ATMOSPHERIC SCIENCES, VOL. 31, SEPTEMBER 2014, 1065–1078

A Generalized Frontogenesis Function and Its Application

YANG Shuai*[1], GAO Shouting[1,2], and LU Chungu[3]

[1]*Laboratory of Cloud-Precipitation Physics and Severe Storms, Institute of Atmospheric Physics, Chinese Academy of Sciences, Beijing* 100029

[2]*State Key Laboratory of Severe Weather, Chinese Academy of Meteorological Sciences, Beijing* 100081

[3]*U.S. National Science Foundation, Arlington, VA* 22230, *USA*

(Received 9 December 2013; revised 20 February 2014; accepted 31 March 2014)

ABSTRACT

With the definition of generalized potential temperature, a new generalized frontogenesis function, which is expressed as the Lagrangian change rate of the magnitude of the horizontal generalized potential temperature gradient, is derived. Such a frontogenesis function is more appropriate for a real moist atmosphere because it can reflect frontogenesis processes, in which the atmosphere in a frontal zone is typically characterized by neither completely dry nor uniform saturation. Furthermore, by derivation, the expression of generalized frontogenesis function includes both temperature and humidity gradients, which is different from and superior to the traditional frontogenesis function in moist processes, which also uses equivalent potential temperature. Diagnostic studies of real cases are performed and show that the generalized frontogenesis function in non-uniformly saturated moist atmosphere indeed provides a useful tool for frontogenesis, compared to using the traditional frontogenesis function. The new frontogenesis function can be used in situations involving either a strong temperature or moisture gradient and is closely correlated with precipitation.

Key words: frontogenesis, diagnostic analysis, case study

Citation: Yang, S., S. T. Gao, and C. G. Lu, 2014: A generalized frontogenesis function and its application. *Adv. Atmos. Sci.*, **31**(5), 1065–1078, doi:10.1007/s00376-014-3228-y.

1. Introduction

Because of the significance of fronts in weather analysis and forecasting, the theory of frontogenesis has been studied extensively for several decades. Bergeron (1928) made a dynamical interpretation of frontogenesis and frontolysis. Newton (1954) studied frontogenesis and frontolysis as a three-dimensional process. Reed (1955) analyzed the characteristic types of upper-level frontogenesis. However, one of the issues facing these earlier studies of fronts was how to suitably define a front and how to depict frontogenesis. From a kinematic point of view, Petterssen (1936) and Miller (1948) discussed the change of front intensity by analyzing the Lagrangian rate of change of a potential temperature gradient, $d|\nabla\theta|/dt$.

Along with the above definition, frontogenesis has been widely discussed. Petterssen (1956) pointed out that vorticity, divergence and deformation all contribute to frontogenesis. Sawyer (1956) derived a frontal secondary circulation equation by adopting a geostrophic approximation with the assumption of no change in potential temperature along the front. Eliassen (1962) further developed the equation by taking into account the change in potential temperature along a front. Hoskins and Bretherton (1972) proposed a semi-geostrophic model depicting nonlinear baroclinic waves and frontogenesis, and demonstrated analytically how the Eady wave could make temperature be discontinuous within a limited time. Based on isentropic potential vorticity (IPV), Fulton and Schubert (1991) developed a frontogenesis theory via isentropic and geostrophic coordinate transformations. Ninomiya (1984, 2000) showed that the deformation and horizontal convergence in the subtropical zone are primary contributors to mei-yu (the East Asian rainy season) frontogenesis. In particular, Ninomiya (1984) argued that, different from polar frontogenesis in which a gradient of potential temperature is conventionally used, a measure of frontogenesis in the mei-yu rainband should adopt a gradient of equivalent potential temperature. Wu et al. (2004) discussed the intensity change of frontal systems by utilizing both local and Lagrangian frontogenesis functions, and then further studied the problem of geostrophic adjustment during frontogenesis. Cohen and Schultz (2005) constructed a framework for diagnosing airstream boundaries (e.g., drylines, lee troughs), beginning with a kinematic expression for the rate of change in the separation vector between two adjacent air parcels. This is similar to a kinematic framework for diagnosing frontogenesis in the form of the Petterssen frontogenesis function and its

* Corresponding author: YANG Shuai
Email: ys_ys@126.com

vector generalization. They are then applied to simple, idealized, steady-state flows and a nonsteady idealized vortex in nondivergent, diffluent flow to determine the characteristics of air-parcel trajectories and airstream boundaries.

The above analyses of frontogenesis cover many aspects. A large number of these studies concentrated on the Lagrangian change in the potential temperature gradient as a criterion for frontogenesis/frontolysis (Petterssen, 1936, 1956; Davies-Jones, 1982, 1985; Doswell, 1984; Keyser et al., 1986; Wu et al., 2004; Ran and Chu, 2007; Li et al., 2013). These theories had some limitations in cases where moisture contrast is larger than the temperature gradient in frontal development. Latent heat release inevitably poses important effects on frontogenesis. Diagnoses using a frontogenesis function based on the measure of $|\nabla\theta|$ may not capture the essence of the physical processes for frontogenesis.

Yu et al. (1995) shed light on the contributions of latent heat to a narrow ascending motion along a front. They pointed out that latent heat release intensifies the gradient of temperature within the cold frontal zone, as well as the cyclonical shear of the wind vector, which tends to increase the intensity of frontal circulation, especially in the ascending branch. Barth and Parsons (1996) pointed out the significance of ice-phase processes in the maintenance of a cold front. By considering ice-phase microphysical processes, sublimation and melting of frozen hydrometeors produced cooling, which further increased the depth and intensity of the cold air mass. Therefore, diabatic cooling within the cold air could potentially play a role in maintaining or even intensifying the circulations that induce precipitation. Wang et al. (2002) conducted a sensitivity experiment of frontogenesis/frontolysis by using an atmospheric numerical model. Their results showed that the frontal intensity (measured by the maximum horizontal gradient of potential temperature) took on a damping tendency in dry atmosphere because of a deficiency in the large-scale frontogenesis mechanism in the initial conditions. In moist atmosphere, meanwhile, its intensity could be maintained for a longer period. These studies stressed the importance of moisture during development of fronts in a moist atmosphere. Therefore, the effect of water vapor should be considered in the frontogenesis process. As discussed previously, a conventional way to incorporate the moisture effect is to replace θ by equivalent potential temperature θ_e in the frontogenesis function, i.e., to use the Lagrangian change of $|\nabla\theta_e|$ as an alternative to measure the frontogenesis (Ninomiya, 1984). However, such an approach sometimes still encounters problems. Using θ_e assumes the atmosphere is saturated, while in the development of a frontal system the atmosphere is typically non-uniformly saturated. Furthermore, as we show in the cases analyzed in this study, using an absolute value of equivalent potential temperature gradient tends to give a front with a relatively weak and loose structure in comparison with observations.

So, what has been missed? Fronts typically develop at the boundaries of two different air masses, such as when a continental polar (CP) air mass meets a maritime tropical (MT) air mass. CP air is dry and cold, while MT air is moist and warm. Using a completely dry measure (e.g., $|\nabla\theta|$) or a completely saturated measure (e.g., $|\nabla\theta_e|$) evidently captures only the two extreme scenarios. Along the frontal boundary, air is most likely non-uniformly saturated. In this study, we propose a new frontogenesis function to account for a more realistic moist weather situation. By applying this new frontogenesis function, we try to gain an understanding of what the role is of the development of the moisture field in facilitating the formation of fronts. In section 2, the generalized frontogenesis function in non-uniformly saturated moist atmosphere is defined; its physical interpretation and an alternative form are given in sections 3 and 4; case studies are performed in section 5; and conclusions are drawn in section 6.

2. The generalized frontogenesis function in non-uniformly saturated moist atmosphere

As discussed above, traditionally, the Lagrangian change in the absolute gradient of θ or T (potential temperature or temperature) is used as the criterion for frontogenesis in a dry atmosphere. In a saturated moist atmosphere, frontogenesis can be defined when θ_e isolines are compacted. However, the real atmosphere is neither absolutely dry nor completely saturated. It is typically non-uniformly saturated, such as near a humidity front.

The rational for the critical concept of "non-uniform saturation" is further explained as follows. The relative humidity within a grid box is not uniform, but patchy and intermittent. Physically, of course, a parcel of air is either unsaturated or fully saturated, with nothing in between. The concept of "non-uniform saturation" allows for the reality that in a grid box of perhaps 100 km on one side, there will be some patches of cloud even when the average relative humidity in the box is less than 100%. "Non-uniform saturation" has been discussed in previous studies by Gao et al. (2004) and Gao and Cao (2007). In fact, it can be understood as "patchy saturation". In this paper, a volume of air that consists of irregular clumps of saturated air embedded in dry air is said to have non-uniform saturation (or patchy saturation).

Furthermore, the real frontogenesis process is accompanied by the approach and mixture of cold-dry and warm-moist flows, which leads to a kind of relatively complicated environmental atmosphere: a non-uniformly saturated atmosphere. Our previous study (Gao et al., 2010, Fig. 6) provided evidence for this process. In detail, a Lagrangian particle dispersion model (Flexpart) is used to trace the approach and mixture of two airflows with different properties. During the Flexpart simulation, downward cold-dry air from upper levels and a lower-level origin of upward warm-moist convection are collocated with each other. Ten thousand particles are released. Then, the hourly distribution of air parcels after dispersion is analyzed. From the zonal-vertical cross section of dispersed air parcels, it is found that warm-moist airflow in the lower troposphere gradually stretches upward. The eastward cold-dry air parcels extend downward. The approaching of a downward cold-dry air originating from the upper levels

and its mixing with the lower-level upward-moving moist air is very clear from the results (Gao et al., 2010, Fig. 6). In addition, it is easy to understand that the process further leads to a non-uniform saturation frontogenesis.

The generalized potential temperature, θ^* (Gao et al., 2004, 2005; Yang et al., 2007; Ran et al., 2010; Wu et al., 2011), can only describe this kind of non-uniformly saturated situation. As a key factor for non-uniformly saturated atmosphere, it is introduced in this study, expressed as

$$\theta^* = \theta \exp\left[\frac{Lq_s}{c_pT}\left(\frac{q}{q_s}\right)^k\right], \tag{1}$$

where θ is potential temperature, T is temperature, q and q_s are specific humidity and saturated specific humidity, exponent k is a tuning parameter, c_p is the specific heat of dry air at constant pressure, and L is the latent heat of condensation. In this expression, the generalized potential temperature is a function of temperature, potential temperature, and humidity, i.e., $\theta^* = \theta^*(T,\theta,q)$. Notice that $q_s = q_s(T)$ exclusively. One can see that in the case of completely dry atmosphere, $q = 0$, Eq. (1) reduces to $\theta^* = \theta$. When the atmosphere is uniformly saturated everywhere, $q = q_s$, Eq. (1) recovers the situation with $\theta^* = \theta_e$. By such a method of parameterization of equivalent potential temperature, the introduction of $(q/q_s)^k$ fixes the discontinuity of the latent heat term in the thermodynamic equation. Instead, a smooth transition between completely dry and uniformly saturated air is achieved through the change in specific humidity from q to q_s. Furthermore, the generalized potential temperature varies smoothly across the saturation threshold. Gao and Cao (2007) also proved its conservation property in moist adiabatic flow, not considering the turbulence mixing effect etc. Certainly, $(q/q_s)^k$ may not be the only form of parameterization of equivalent potential temperature. Since this form has been proved feasible in the application of θ^* and generalized moist potential vorticity (GMPV) to track cyclones (Gao and Cao, 2007), non-uniformly saturated Q vector (Yang et al., 2007), the modified convective vorticity vector (Yang and Wang, 2009), non-uniformly saturated stability (Yang and Gao, 2006; Yang et al., 2009) etc., we adopt it in this study.

Using this generalized potential temperature, a new generalized frontogenesis function in a non-uniformly saturated moist atmosphere (termed the "non-uniformly saturated frontogenesis function"), is defined as

$$F = \frac{d}{dt}|\nabla\theta^*|, \tag{2}$$

which measures the Lagrangian rate of change in the absolute value of a horizontal gradient of the generalized potential temperature. Of course, in completely dry atmosphere, Eq. (2) reduces to the classic frontogenesis function, $F = d|\nabla\theta|/dt$. In this case, there is no connection between frontogenesis and moisture processes because F is not a function of q and q_s. Furthermore, in a completely saturated atmosphere, Eq. (2) becomes the moist frontogenesis function, $F = d|\nabla\theta_e|/dt$. In this case, although moisture enters the frontal dynamics, only saturated atmosphere, q_s, contributes to the frontogenesis. The continuous variation of the moisture field is not captured in the frontal development. Note that F is not a function of q. Above absolutely dry and saturated moist flows are extreme cases. In the moist but unsaturated region, $0 < q < q_s, 0 < (q/q_s)^k < 1, \theta^* \neq \theta$ and $\theta^* \neq \theta_e$, and $F = d|\nabla\theta^*|/dt$ is a function of θ, q and q_s. Therefore, we substitute the expression of θ^* into the frontogenesis expression and fully expand the result to show how it generalizes all situations by posing itself as a function of θ, q, and q_s, and how it depends on the gradients of θ, q, and q_s in non-uniformly saturated moist flow.

Since $O(\Delta T) \ll O(T), O(\Delta q_s) \sim O(q_s)$, we have $O(\nabla T/T) \ll O(\nabla q_s/q_s)$, where the units of T and q_s are K and kg kg^{-1}, respectively. With these relations, substituting the expression of θ^* [Eq. (1)] into the frontogenesis function [Eq. (2)], the non-uniformly saturated frontogenesis function can be expanded as

$$F = \frac{d}{dt}|\nabla\theta^*| = \frac{d}{dt}|\theta^*(F_\theta + F_q)|, \tag{3}$$

where

$$F_\theta = \frac{1}{\theta}\nabla\theta, \tag{4a}$$

$$F_q = \frac{L}{c_pT}\nabla\left[q_s\left(\frac{q}{q_s}\right)^k\right]. \tag{4b}$$

To show the relative importance of $\nabla\theta, \nabla T, \nabla q$, and ∇q_s in F, the order of magnitude for each term in Eq. (3) is estimated as follows. It is shown that the correlation between F and ∇q depends on the relative humidity, r.

If taking $O(\theta) \sim 10^2$ K, $O(T) \sim 10^2$ K, $O(\Delta\theta) \sim 10^1$ K, $O(\Delta T) \sim 10^1$ K, $L = 2.5 \times 10^6$ J kg^{-1}, $c_p = 1.005 \times 10^3$ J kg^{-1} K^{-1}, $O(q) \sim 5 \times 10^{-2}$ kg kg^{-1}, $O(q_s) \sim 5 \times 10^{-2}$ kg kg^{-1}, $O(\Delta q) \sim 5 \times 10^{-2}$ kg kg^{-1}, $O(\Delta q_s) \sim 5 \times 10^{-2}$ kg kg^{-1}, and $(q/q_s)^k$ values are shown in Fig. 1. When $r = 75\%$, $F_\theta \sim F_q$. For a typical synoptic-scale front, if the relative humidity is greater (less) than 75%, then the F_θ term is less (greater) than the F_q term. These analyses indicate, by reference to Eq. (3), that in the region with high relative humidity, F is more sensitive to the moisture gradient; while in the region with low relative humidity, F is more sensitive to

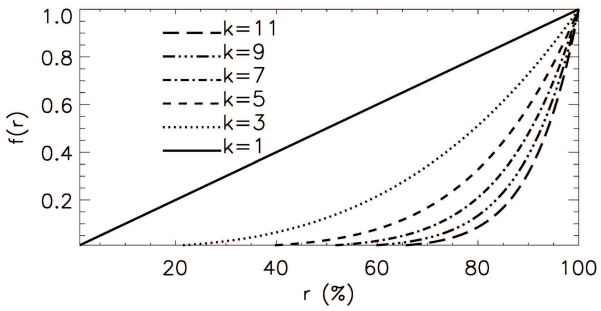

Fig. 1. A plot of weighting function, $f(r)$, as a function of r, where $r = q/q_s$ is relative humidity and $f(r) = (q/q_s)^k$.

the temperature gradient. In the vicinity of $r = \sim 75\%$, both the temperature and moisture gradients are important to F, which is demonstrated by the case study in section 5.

We now address the issue of how one should determine the tuning parameter, k, in the weighting function that we introduced in the non-uniformly saturated frontogenesis function. The implicit assumption we make here is that frontogenesis due to moist processes only takes an effect when condensation occurs. Mason (1971) suggested that, during cloud formation, condensation typically occurs when relative humidity reaches 75%. Zhao and Carr (1997) also empirically set the critical value of relative humidity for condensation to 75% over land by their sensitivity experiments. Based on these observational studies, we plot our weighting function as a function of relative humidity for various k values (Fig. 1). One can see that for $k = 1, 3, 5$, the weighting function takes an effective threshold [a non-zero value, say $f(r) = 0.1$] at somewhat premature relative humidity values, i.e., 8%, 43%, 60%. When $k = 9$, the threshold of the weighting function occurs correctly at the 75% relative humidity value. Based on this analysis, it is advisable that a reasonable value of $k = 9$ should be adopted in the cloud formation related to frontal processes.

The absolute value of a horizontal gradient of generalized potential temperature is calculated by

$$|\nabla\theta^*| = \sqrt{\left(\frac{\partial\theta^*}{\partial x}\right)^2 + \left(\frac{\partial\theta^*}{\partial y}\right)^2}\,. \tag{5}$$

Using this definition, we can next analyze in detail the non-uniformly saturated frontogenesis function.

Substituting Eq. (5) into Eq. (2), one can derive

$$F = \frac{d}{dt}|\nabla\theta^*| = \frac{1}{|\nabla\theta^*|}\left[\frac{\partial\theta^*}{\partial x}\frac{d}{dt}\left(\frac{\partial\theta^*}{\partial x}\right) + \frac{\partial\theta^*}{\partial y}\frac{d}{dt}\left(\frac{\partial\theta^*}{\partial y}\right)\right]. \tag{6}$$

Given $d\theta^*/dt = Q^*$, the following relations can be obtained:

$$\frac{d}{dt}\left(\frac{\partial\theta^*}{\partial x}\right) = -\frac{\partial \boldsymbol{V}_\mathrm{h}}{\partial x}\cdot\nabla\theta^* - \frac{\partial\omega}{\partial x}\frac{\partial\theta^*}{\partial p} + \frac{\partial Q^*}{\partial x}\,, \tag{7a}$$

$$\frac{d}{dt}\left(\frac{\partial\theta^*}{\partial y}\right) = -\frac{\partial \boldsymbol{V}_\mathrm{h}}{\partial y}\cdot\nabla\theta^* - \frac{\partial\omega}{\partial y}\frac{\partial\theta^*}{\partial p} + \frac{\partial Q^*}{\partial y}\,, \tag{7b}$$

where $\boldsymbol{V}_\mathrm{h} = u\boldsymbol{i} + v\boldsymbol{j}$ is horizontal velocity, ω is the vertical velocity in the p-coordinate system, and Q^* is the diabatic heating excluding latent heat, such as the radiative heating due to solar and infrared radiation and other heating/cooling effects.

Substituting these relations, Eq. (6) becomes

$$F = -\frac{1}{|\nabla\theta^*|}\left[\frac{\partial\theta^*}{\partial x}\left(\frac{\partial \boldsymbol{V}_h}{\partial x}\cdot\nabla\theta^*\right) + \frac{\partial\theta^*}{\partial y}\left(\frac{\partial \boldsymbol{V}_h}{\partial y}\cdot\nabla\theta^*\right)\right] - \frac{1}{|\nabla\theta^*|}\left[(\nabla\theta^*\cdot\nabla\omega)\frac{\partial\theta^*}{\partial p}\right] + \frac{1}{|\nabla\theta^*|}(\nabla\theta^*\cdot\nabla Q^*)\,. \tag{8}$$

It can be seen from Eq. (8) that the non-uniformly saturated frontogenesis function is associated with the contributions of horizontal motion, vertical motion and diabatic heating. These physical processes are examined in detail in the next section.

3. Analysis of physical processes related to frontogenesis in a non-uniformly saturated atmosphere

3.1. *The contribution of horizontal motion to frontogenesis*

For the convenience of discussion, the θ^* isolines are assumed to be parallel to the x-axis. Thus, the y-axis points to the direction of the gradient of θ^*, and $\partial\theta^*/\partial x = 0$, $\partial\theta^*/\partial y = \nabla\theta^*$. Under this setup, the terms related to horizontal motion,

$$-\frac{1}{|\nabla\theta^*|}\left[\frac{\partial\theta^*}{\partial x}\left(\frac{\partial \boldsymbol{V}_h}{\partial x}\cdot\nabla\theta^*\right) + \frac{\partial\theta^*}{\partial y}\left(\frac{\partial \boldsymbol{V}_h}{\partial y}\cdot\nabla\theta^*\right)\right],$$

become

$$-\frac{1}{|\nabla\theta^*|}\left[\left(\frac{\partial\theta^*}{\partial y}\right)^2\frac{\partial v}{\partial y}\right].$$

Because v is the velocity component along the y-axis, it is orthogonal to θ^* isolines. As v decreases along the orientation of the horizontal gradient of θ^*, i.e.,

$$\frac{\partial v}{\partial y} < 0, \quad -\frac{1}{|\nabla\theta^*|}\left[\left(\frac{\partial\theta^*}{\partial y}\right)^2\frac{\partial v}{\partial y}\right] > 0$$

(a positive contribution to F), frontogenesis presents. On the contrary, when

$$\frac{\partial v}{\partial y} > 0, \text{ and thus } -\frac{1}{|\nabla\theta^*|}\left[\left(\frac{\partial\theta^*}{\partial y}\right)^2\frac{\partial v}{\partial y}\right] < 0$$

(a negative contribution to F), frontolysis occurs. These effects manifest the contribution of horizontal motion to frontogenesis: θ^* isolines contract/expand in response to horizontal convergence/divergence.

3.2. *The contribution of vertical motion to frontogenesis*

Similar to the terms associated with horizontal velocity, the isolines of θ^* are also assumed to be parallel with the x-axis. Therefore, the terms related to vertical motion,

$$-\frac{1}{|\nabla\theta^*|}\left[(\nabla\theta^*\cdot\nabla\omega)\frac{\partial\theta^*}{\partial p}\right],$$

become

$$-\frac{1}{|\nabla\theta^*|}\left(\frac{\partial\theta^*}{\partial y}\frac{\partial\omega}{\partial y}\frac{\partial\theta^*}{\partial p}\right),$$

which renders $(\partial\omega/\partial y)(\partial\theta^*/\partial p)$. In stable stratification (i.e., $\partial\theta^*/\partial p < 0$), if a warm and moist air parcel ascends ($\omega < 0$) and the cold and dry air descends ($\omega > 0$), which leads to $\partial\omega/\partial y > 0$, the contribution of vertical motion to frontogenesis is negative, i.e., $(\partial\omega/\partial y)(\partial\theta^*/\partial p) < 0$ (a negative contribution to F), and frontolysis presents. Frontogenesis presents for the opposite case when warm air descends and cold air ascends $(\partial\omega/\partial y)(\partial\theta^*/\partial p) > 0$, a positive contribution to F). For unstable stratification, frontogenesis/frontolysis presents for the opposite y-gradient coupling of vertical motion to that for stable stratification.

3.3. *The contribution of diabatic heating to frontogenesis*

The terms related to diabatic heating, $(\nabla\theta^*\cdot\nabla Q^*)/|\nabla\theta^*|$, can be simplified to

$$\frac{1}{|\nabla\theta^*|}\left(\frac{\partial\theta^*}{\partial y}\frac{\partial Q^*}{\partial y}\right),$$

which will result in $-\partial Q^*/\partial y$, under the above assumption. As the cold air moves southward and reaches above warm air, the heat will be transferred into the cold atmosphere by physical processes such as the radiative heating due to solar and infrared radiation and other heating/cooling effects, which makes cold air become warmer, and the generalized potential temperature increases, i.e., $d\theta^*/dt > 0 (Q^* > 0)$. The diabatic heat changes the property of the cold air, which leads to the descending gradient of generalized potential temperature between cold and warm air, $-\partial Q^*/\partial y < 0$, and frontolysis presents. Similarly, as warm air moves northwards and diabatic cooling occurs, then $d\theta^*/dt < 0 (Q^* < 0)$, which also leads to a decrease in the gradient of generalized potential temperature, and $-\partial Q^*/\partial y < 0$, and therefore frontolysis presents.

4. An alternative form of the non-uniformly saturated frontogenesis function

Using Eqs. (6), (7a) and (7b), we can reorganize terms to write F in the form

$$F = F_1 + F_2 + F_3 + F_4 \,, \tag{9}$$

with

$$F_1 = -\boldsymbol{n}\cdot\nabla Q^* \,, \tag{10a}$$

$$F_2 = \frac{\partial\theta^*}{\partial p}\boldsymbol{n}\cdot\nabla\omega \,, \tag{10b}$$

$$F_3 = -\frac{D}{2}|\nabla\theta^*| \,, \tag{10c}$$

$$F_4 = -\frac{1}{2|\nabla\theta^*|}\left[E_{\rm st}\left(\frac{\partial\theta^*}{\partial x}\right)^2 + 2E_{\rm sh}\left(\frac{\partial\theta^*}{\partial x}\frac{\partial\theta^*}{\partial y}\right) - E_{\rm st}\left(\frac{\partial\theta^*}{\partial y}\right)^2\right], \tag{10d}$$

where $\boldsymbol{n}$ is a unit vector along the direction of $(-\nabla\theta^*)$. $D = (\partial u/\partial x + \partial v/\partial y)$ is horizontal divergence, $E_{\rm st} = (\partial u/\partial x - \partial v/\partial y)$ is stretch deformation, and $E_{\rm sh} = (\partial v/\partial x + \partial u/\partial y)$ is shear deformation.

Ninomiya (1984, 2000) derived the above relations for a traditional frontogenesis function. We arrived at similar forms of these equations, except with θ^* replacing θ_e. However, this substitution generalizes the frontogenesis process in a background atmosphere from complete saturation to non-uniform saturation. The physical meaning of each term in Eq. (9) is now analyzed.

4.1. *The term related to diabatic heating,* F_1

F_1 represents the contribution of diabatic heating to frontogenesis, which is given by the projection of the horizontal gradient of diabatic heating onto the direction of the horizontal gradient of generalized potential temperature.

4.2. *The vertical motion term,* F_2

F_2 represents the contribution of vertical motion to frontogenesis. This effect is measured by the projection of the horizontal gradient of vertical velocity onto the direction of the horizontal gradient of generalized potential temperature.

In stable stratified atmosphere ($\partial\theta^*/\partial p < 0$), the coupling between descent of warm air ($\omega > 0$) and the ascent of cold air ($\omega < 0$) will lead to $\boldsymbol{n}\cdot\nabla\omega < 0$, so that $F_2 > 0$, and frontogenesis occurs, and vice versa.

4.3. *The horizontal convergence/divergence term,* F_3

F_3 represents the increase or decrease of the horizontal gradient of generalized potential temperature (i.e., the frontogenesis or frontolysis processes) induced by horizontal convergence ($D < 0$) or divergence ($D > 0$).

4.4. *The horizontal deformation term,* F_4

F_4 denotes the contribution of horizontal deformation to frontogenesis. To simplify the analysis of this term, an ideal state is given. We assume adiabatic ($F_1 = 0$) and horizontal airflow ($F_2 = 0$) (e.g., on a rigid horizontal boundary, just like terrestrial external surfaces). A typical deformation field (e.g., pure stretch deformation) is considered here as an example. The assumption is taken so that the shearing deformation vanishes locally. Let us take x as the axis of dilatation and y as the axis of contraction. The angle between generalized potential temperature and the x-axis is β (Fig. 2), and thus the angle between $-\nabla\theta^*$ and the x-axis is $\phi = \beta + \pi/2$. The gradient of generalized potential temperature is expressed as

$$-\nabla\theta^* = |\nabla\theta^*|[(-\sin\beta)\boldsymbol{i} + \cos\beta\,\boldsymbol{j}] \,, \tag{11}$$

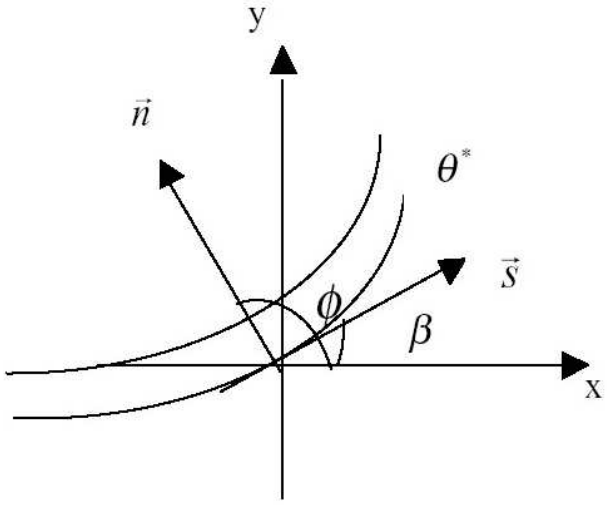

Fig. 2. Schematic illustration of right-hand Cartesian coordinate systems, (x,y) and (s,n), defined locally by rotating the standard (x,y) Cartesian coordinates system through angles β into the (s,n) system. The s-axis is tangent to an isoline of θ^* and is directed such that the n-axis points towards colder air. The angle between $\boldsymbol{n}$ and the x-axis is ϕ.

which indicates

$$\frac{\partial\theta^*}{\partial x} = |\nabla\theta^*|\sin\beta\ , \quad \frac{\partial\theta^*}{\partial y} = -|\nabla\theta^*|\cos\beta\ . \tag{12}$$

Combining Eq. (12) with Eq. (10d), the expression for F_4 becomes

$$F_4 = \frac{|\nabla\theta^*|}{2}(E_{\rm st}\cos 2\beta + E_{\rm sh}\sin 2\beta)\ . \tag{13}$$

For pure stretch deformation (shear deformation $E_{\rm sh} = 0$), Eq. (13) is simplified to

$$F_4 = \frac{1}{2}|\nabla\theta^*|E\cos 2\beta\ , \tag{14}$$

where $E\,(E = \sqrt{E_{\rm st}^2 + E_{\rm sh}^2})$ is total deformation.

For $\beta < \pi/4$, $F_4 > 0$, frontogenesis occurs; whereas, for $\beta = \pi/4, F_4 = 0$, and for $\beta > \pi/4, F_4 < 0$, frontolysis is more favorable. However, the θ^* isolines will rotate to $\beta < \pi/4$ in the deformation-dominated flow, i.e., it turns to frontogenesis. As $\beta = 0$, the frontogenesis reaches its peak in strength. Therefore, deformation is the most favorable frontogenesis pattern flow.

Combining Eqs. (10) and (14), in typical "saddle" flow pattern (i.e., $E_{\rm sh} = 0$), if not considering the diabatic heating, $F_i(i = 1, \cdots, 4)$ becomes

$$F_1 = 0\ , \tag{15a}$$

$$F_2 = \theta^*\left\{\frac{1}{\theta}\frac{\partial\theta}{\partial p} + \frac{\partial}{\partial p}\left[\frac{Lq_s}{c_pT}\left(\frac{q}{q_s}\right)^k\right]\right\}\boldsymbol{n}\cdot\nabla\omega\ , \tag{15b}$$

$$F_3 = -\frac{D}{2}\theta^*\left|\left\{\frac{1}{\theta}\nabla\theta + \nabla\left[\frac{Lq_s}{c_pT}\left(\frac{q}{q_s}\right)^k\right]\right\}\right|\ , \tag{15c}$$

$$F_4 = \frac{1}{2}\theta^*\left|\left\{\frac{1}{\theta}\nabla\theta + \nabla\left[\frac{Lq_s}{c_pT}\left(\frac{q}{q_s}\right)^k\right]\right\}\right|E\cos 2\beta\ . \tag{15d}$$

From Eqs. (15a–d), one can see that in a non-uniformly saturated atmosphere, the frontogenesis depends not only upon the temperature (or potential temperature) gradient, ∇T or $\nabla\theta$, but also upon the moisture gradient, ∇q. Note that q_s is a function of temperature only. Therefore, the current generalization of the frontogenesis function using generalized potential temperature can be used in real atmospheric conditions to capture frontogenesis due to the change of temperature as well as moisture fields.

In a completely dry atmosphere, $q = 0, (q/q_s)^k = 0, \theta^* = \theta, F_i(i = 2,3,4)$ are not functions of q and q_s. Thus, $F_i(i = 2,3,4)$ are reduced to

$$F_2 = \frac{\partial\theta}{\partial p}\boldsymbol{n}'\cdot\nabla\omega\ ,\ F_3 = -\frac{D}{2}|\nabla\theta|\ ,\ \text{and}\ F_4 = \frac{1}{2}|\nabla\theta|E\cos 2\beta'\ , \tag{16}$$

where $\boldsymbol{n}'$ is a unit vector along the direction of $(-\nabla\theta)$, and β' represents the angle between potential temperature and the x-axis. Equation (16) represents the terms in the frontogenesis function for dry atmosphere. It is indicated from Eq. (16) that the classic frontogenesis theory describes front development based solely upon the isoline collapse. The contribution of moisture to frontogenesis is not captured by this method.

In completely saturated atmosphere, $q = q_s, (q/q_s)^k = 1, \theta^* = \theta_e, F_i(i = 2,3,4)$ are not a function of q. Thus, Eq. (15) results in the form

$$\begin{aligned} F_2 &= \theta_e\left[\frac{1}{\theta}\frac{\partial\theta}{\partial p} + \frac{\partial}{\partial p}\left(\frac{Lq_s}{c_pT}\right)\right]\boldsymbol{n}''\cdot\nabla\omega\ , \\ F_3 &= -\frac{D}{2}\theta_e\left|\left[\frac{1}{\theta}\nabla\theta + \nabla\left(\frac{Lq_s}{c_pT}\right)\right]\right|\ , \\ F_4 &= \frac{1}{2}\theta_e\left|\left[\frac{1}{\theta}\nabla\theta + \nabla\left(\frac{Lq_s}{c_pT}\right)\right]\right|E\cos 2\beta''\ , \end{aligned} \tag{17}$$

where $\boldsymbol{n}''$ is a unit vector along the direction of $(-\nabla\theta_e)$ and β'' represents the angle between equivalent potential temperature and the x-axis. Equation (17) represents the terms in the frontogenesis function for saturated moist atmosphere.

It can be seen that the difference between Eq. (15) and Eqs. (16) and (17) is the effect of the moisture gradient. Therefore, it is evident that the non-uniformly saturated frontogenesis function diagnoses frontogenesis well in regions with a large moisture gradient. Furthermore, it can be expected that the non-uniformly saturated frontogenesis function can capture the full spectrum of frontal development no matter whether the atmosphere is dry, unsaturated, or saturated.

5. Cases study

In this section, two real atmospheric cases are examined. The application of the newly defined frontogenesis function for a non-uniformly saturated moist atmosphere is conducted by using $1^\circ \times 1^\circ$ National Centers for Environmental Prediction (NCEP) Final (FNL) analysis data. Details of this dataset can be found at http://dss.ucar.edu/datasets/ds083.2/.

5.1. *The two cases*

Case I is from 0000 UTC 12 to 0000 UTC 13 August 2004. The rainbelt in the Huabei region of northern China stretched in the northeast–southwest direction (Fig. 3a). Three precipitation centers were located at (37°N, 113°E), (37.5°N, 114.5°E), and (39°N, 117.5°E). Another patch of heavy rain occurred over the southeast coast of China, associated with an extratropical cyclone. However, we concentrate on the rainband that occurred in the northern part of China. The circulation background over the Huabei region indicates that a line of strong confluence shear and a typical "saddle" pattern existed in the lower troposphere between 30°N and 42°N (Fig. 4a). A large low trough was located to the north of the shear line stretching from (46°N, 126°E) to (40°N, 110°E) with northeast–southwest orientation. The 'saddle' flow pattern stretched vertically upward above the 500 hPa level (not shown). A subtropical anticyclone covered the regions south of the shear line. At the 200 hPa level, directly above the frontal precipitation region (Fig. 3a), divergence flow dominated along the northeast edge of the South Asia

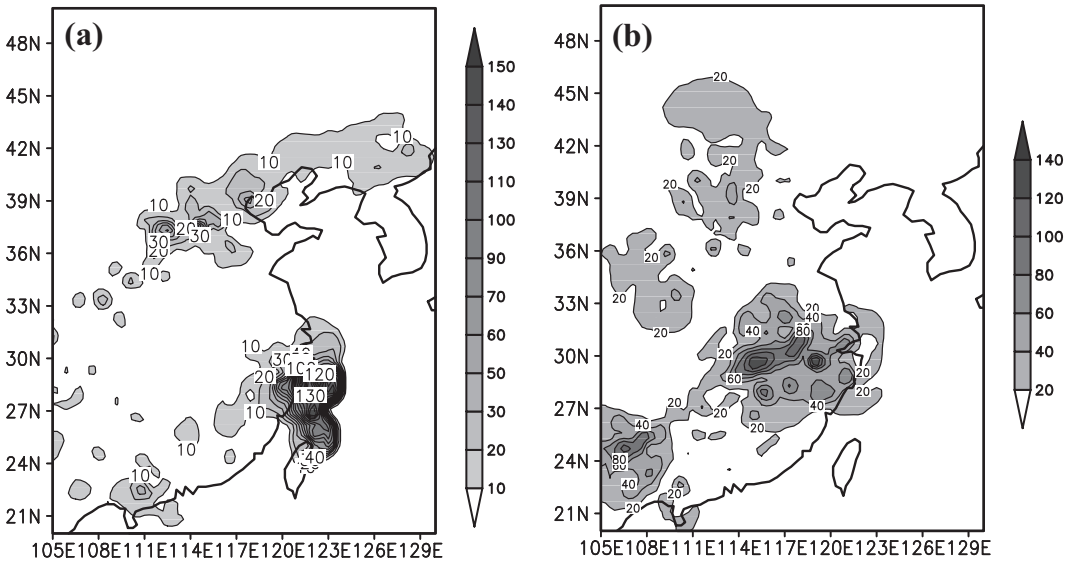

Fig. 3. (a) Observed 24-h total rainfall amount (mm) in north China from 0000 UTC 12 to 0000 UTC 13 August 2004; (b) observed 36-h total rainfall amount (mm) over the middle and lower reaches of the Yangtze River from 0000 UTC 6 July to 1200 UTC 7 July 2003.

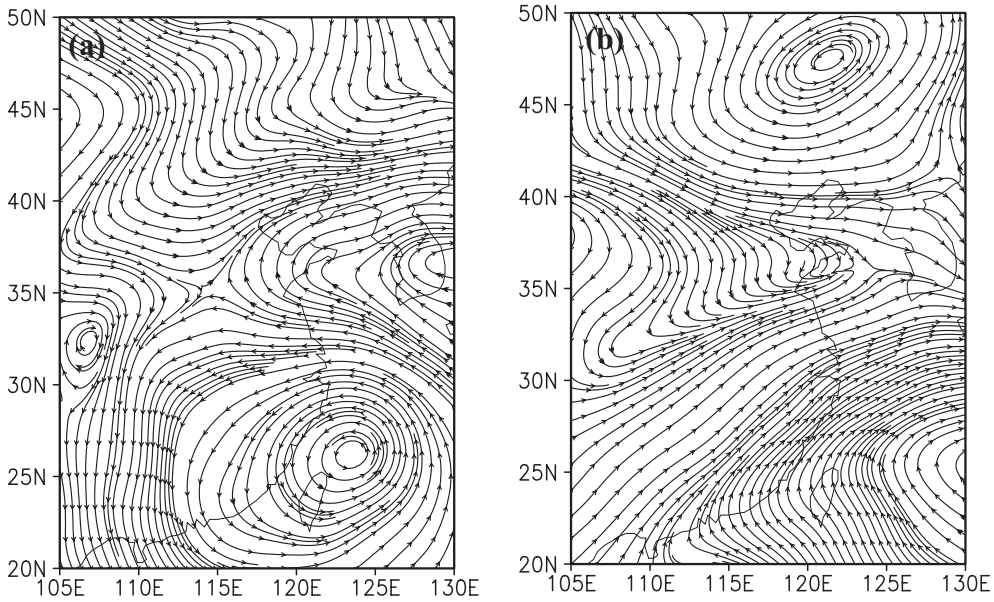

Fig. 4. The streamline field at the 700-hPa level (a) at 0000 UTC 12 August 2004 and (b) 0000 UTC 6 July 2003.

high (not shown).

Another case (Case II) is from 0000 UTC 6 July to 1200 UTC 7 July 2003. A heavy rainfall event associated with a mei-yu front occurred over the middle and lower reaches of the Yangtze River (MRYR) between (24°N, 105°E) and (30°N, 120°E) over China (Fig. 3b). Another area of light rain occurred north of 33°N, associated with a relatively weak front. We concentrate only on the rainband in the MRYR region here. The rainband was oriented in the southwest–northeast direction. A line of strong confluence along with a strong wind shear existed in a northeast–southwest orientation and was located at around 27°–36°N (Fig. 4b). The confluent shear zone was a result of a large-scale flow pattern that consisted of a subtropical high located in the northwestern Pacific at around (25°N, 129°E), a low centered at (48°N, 122°E), and an anticyclonic flow over a large part of China south of the Yangtze River. At 200 hPa, the above rainfall region was dominated by divergence flow (not shown). It is particularly noteworthy that the precipitation along the front tended to present double rainbelts, especially east of 114°E.

5.2. *Frontogenesis analysis in the two cases*

The 6-hourly $1° \times 1°$ NCEP analysis data are used to analyze the characteristics of frontogenesis for the above two precipitation events. Both temperature and humidity (Figs. 5a and b) gradients were formed over the Huabei region (to

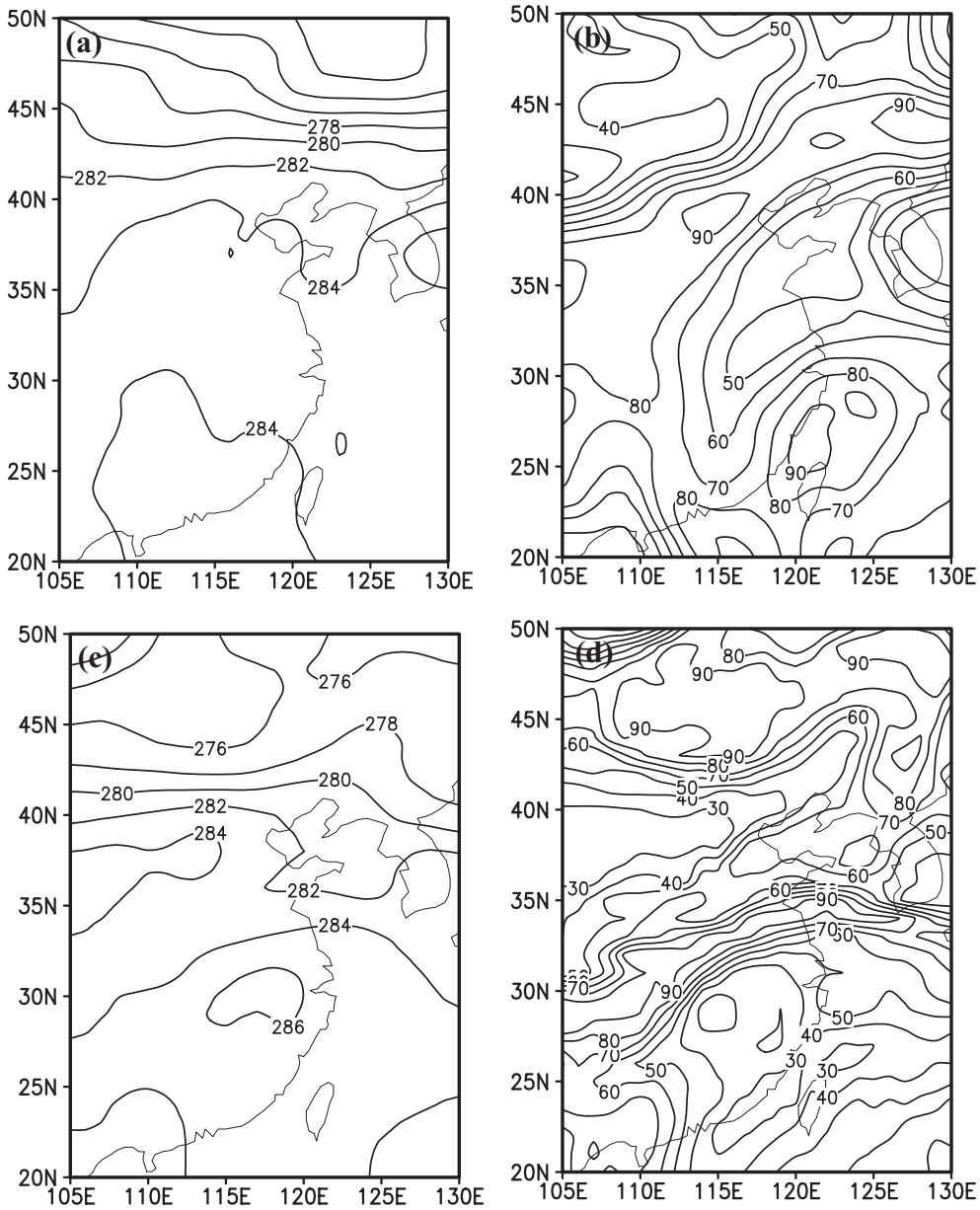

Fig. 5. (a) Temperature (K) and (b) relative humidity (%) at 700 hPa at 0000 UTC 12 August 2004; (c) temperature (K) and (d) relative humidity (%) at 700 hPa at 0000 UTC 6 July 2003.

the north of 36°N) before the onset of precipitation during Case I. Unlike the classical cold/warm front, Case II had a distinctively strong gradient in humidity over the MRYR (Fig. 5d). There was no temperature gradient associated with the rainband (Fig. 5c). Along this moisture front (Fig. 5d), double moisture gradients were evident, which was consistent with the double rainbelts identified in Fig. 3b.

Let us first examine the vertical distribution of generalized potential temperature. Figures 6a–c are the meridional vertical cross sections (along 116°E) of the potential temperature (θ), equivalent potential temperature (θ_e), and generalized potential temperature (θ^*), along with perturbation specific humidity at 0000 UTC 6 July 2003. From the distribution of perturbation specific humidity (Figs. 6a–c), one can see that a large horizontal moisture gradient was located below 300 hPa when crossing the frontal zone between 25°N and 33°N. Because there was little water vapor in the upper troposphere, θ^* had a similar distribution pattern to that of θ in the upper troposphere (compare both at about 300 hPa in Figs. 6c and a). This is coincident with the theoretical analyses in the previous sections. Until the middle and lower troposphere, where the moisture gradient became large across the frontal zone accompanied by the increase in water vapor, the distribution of θ^* and θ lines began to show significant differences. In particular, the θ lines clearly failed to capture the moisture front, while θ^* presented a frontal zone that co-located with the large moisture gradients. In comparison with equivalent potential temperature, the distribution of θ^* lines

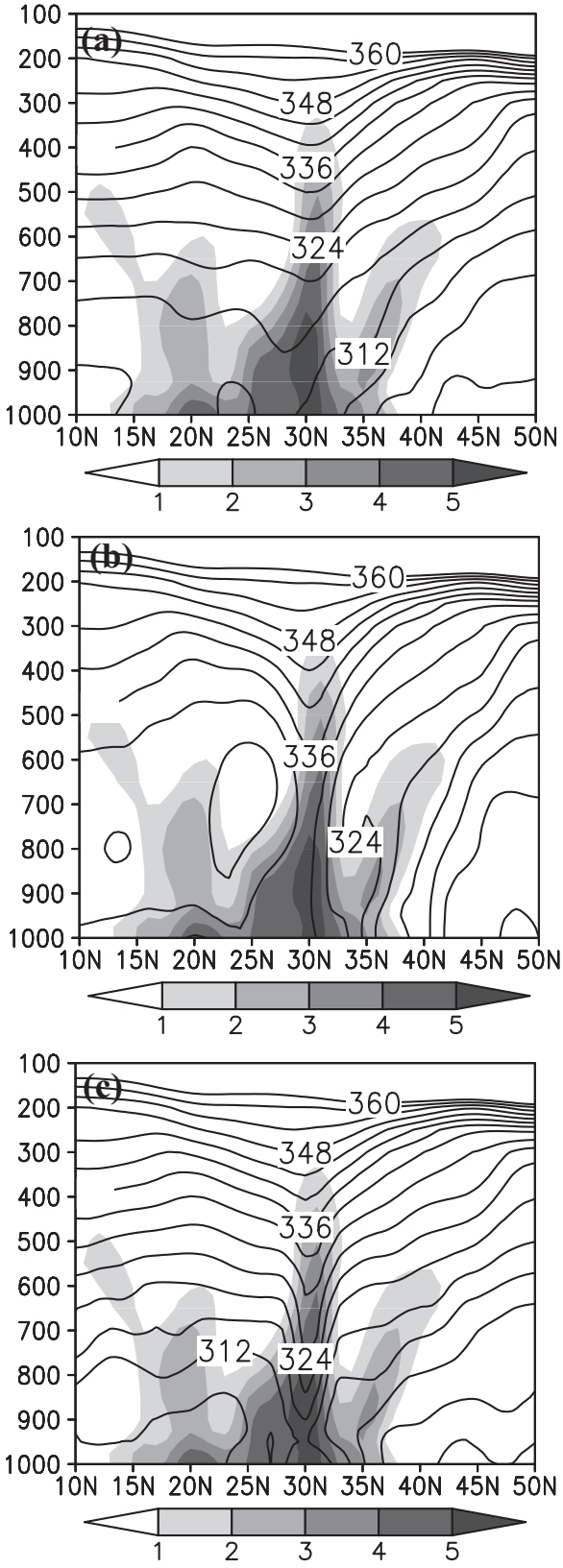

Fig. 6. The meridional vertical cross section along 116°E of (a) potential temperature (θ), (b) equivalent potential temperature (θ_e), (c) generalized potential temperature (θ^*) (K) along with perturbation specific humidity (shaded; g kg^{-1}) at 0000 UTC 6 July 2003.

(Fig. 6c) was similar to that of θ_e lines (Fig. 6b) to a large extent, but θ^* isolines showed a much stronger front than θ_e isolines. The narrow θ^* trough extended downwards in response to the moisture ridge, stretching upwards between 25°N and 33°N (Fig. 6c), right in the region where precipitation occurred. The θ_e trough, on the other hand, did not extend as low as to the surface, and the largest θ_e front occurred on the north side of the moisture front. This is understandable because the θ_e gradient depends on the gradient of saturated moisture, which is typically achieved first on the cool temperature side. The gradient of θ^* on the south side of the moisture ridge (south of 30°N) captured the gradient of moisture that was clearly not saturated (Fig. 6c). Again, this understanding is consistent with the theoretical analyses in the previous sections. Based on the above diagnoses, we can conclude that frontogenesis using θ and θ_e misrepresents the true moist front, while θ^* can represent the frontogenesis process in a non-uniformly saturated atmosphere.

To further demonstrate this, we computed the frontogenesis function using both θ^* and θ_e for Cases I and II. In Fig. 7, we plot the generalized potential temperature (dashed lines in Fig. 7a), and equivalent potential temperature (dashed lines in Fig. 7b), and corresponding frontogenesis functions (gray shading). In general, θ^* tended to generate a much stronger front than θ_e, which may be associated with the effect of more water vapor and induced latent heating release being included in the θ^* formula. Furthermore, the frontogenesis function based on generalized potential temperature presented a better pattern and location for precipitation (e.g., both stretch northeastwards, east of 117°E in Figs. 7a and 3a.) than that based on equivalent potential temperature (compare Figs. 7a and b). From Fig. 7a, the generalized potential temperature and the non-uniformly saturated frontogenesis zones corresponded to fronts (large gradients of both temperature and humidity in Figs. 5a and b) well at 700 hPa, as compared to the equivalent potential temperature and the traditional frontogenesis function (Ninomiya, 1984, 2000) (Fig. 7b), e.g., to the east of 117°E where the large gradients of both temperature and humidity locate.

We also conducted the same analyses for Case II. In Fig. 8, the same fields are plotted as in Fig. 7. Again, we see the frontogenesis function based on θ^* generated a much better front than that based on θ_e. In particular, the double moisture fronts identified in Fig. 5d were presented in the non-uniformly saturated frontogenesis function as well (Fig. 8a), while the front generated by using the equivalent potential temperature was very weak and failed to capture the double-front structure (Fig. 8b). The above analyses further verify the theoretical analyses in sections 2 and 4 that implied the non-uniformly saturated frontogenesis function diagnoses frontogenesis well in regions with a large moisture gradient since its expressions include ∇q.

Furthermore, the cases studies in this section are consistent with the theoretical analyses in section 2 in which the sensitivity of F to θ and q was demonstrated when the temperature and humidity fields are poorly synchronized in the moist process. For example, for the region with high humid-

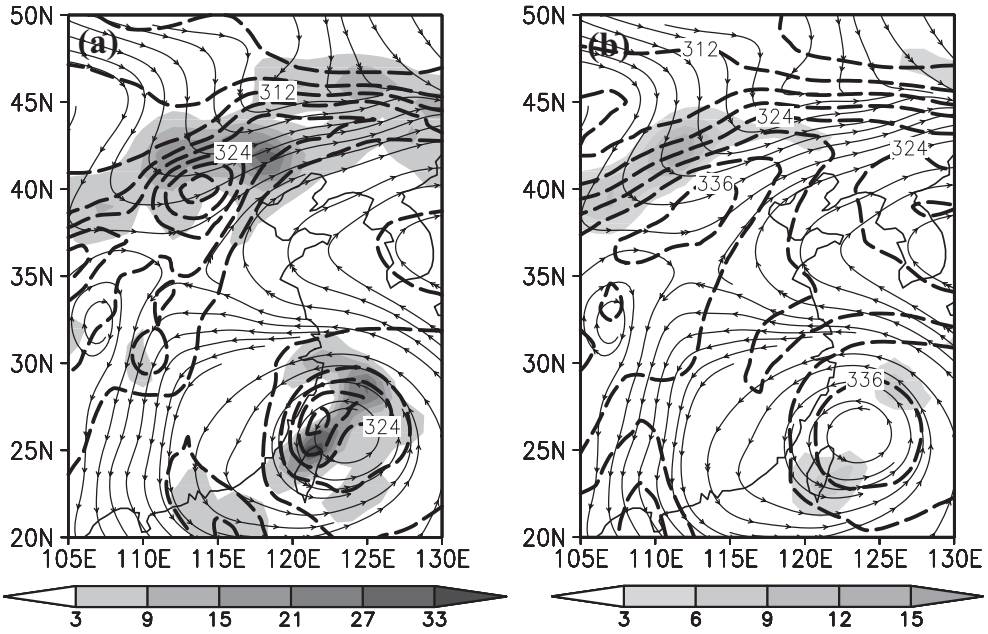

Fig. 7. (a) The generalized potential temperature (dashed lines) and (b) equivalent potential temperature (dashed lines) (units: K) along with corresponding frontogenesis functions (gray shading) (units: 10^{-10} K s^{-1} m^{-1}) and stream line (vectors) at 700 hPa at 0000 UTC 12 August 2004.

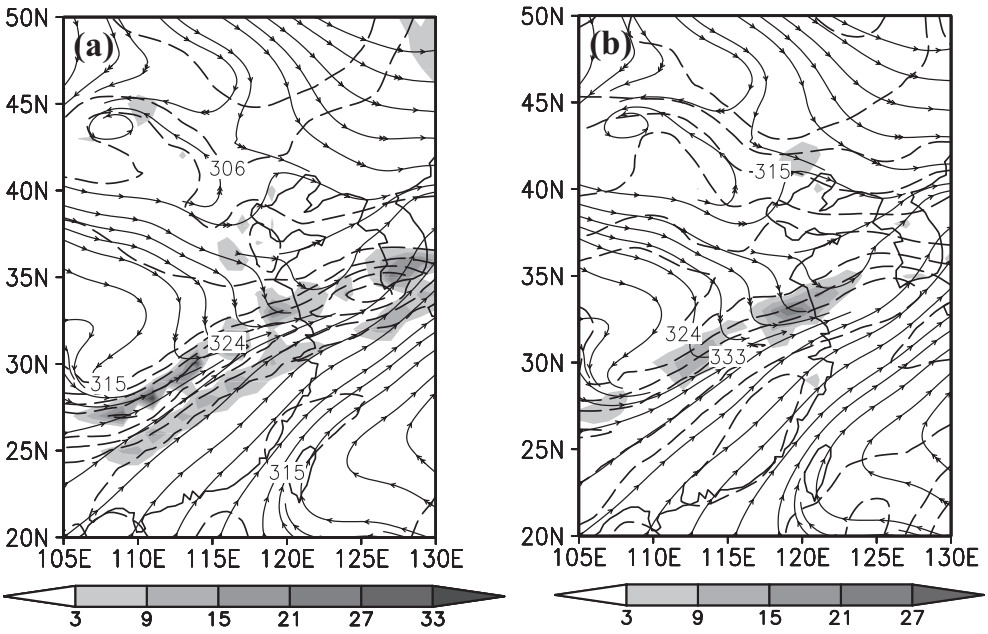

Fig. 8. The same as Fig. 7, except for 0000 UTC 6 July 2003.

ity west of 117°E, and between 36°N and 45°N, F is sensitive to the moisture gradient; while for the regions with relative humidity values less than 75% near 45°N and east of 117°E, F is sensitive to the temperature gradient and can reflect the large temperature gradient in Case I (Figs. 7, 5a and b). Similarly, F is sensitive to the moisture gradient and can reflect the large moisture gradient near 30°N in the regions with relative humidity higher than 75% in Case II (Figs. 8 and 5d). All these analyses prove the theoretical derivation presented in section 2.

To further confirm this analysis, we also plot the meridional vertical sections along 116°E of the non-uniformly saturated frontogenesis function (shaded), streamline field (arrowed lines), θ^* (dashed lines), and precipitation amount (vertical bar lines) at 0000 UTC 6 July 2003 (Fig. 9). Again, the θ^* isolines represented a sharp trough vertically, and the frontogenesis function did split into two bands above the surface, with the north band slightly stronger than the south band. From the discussion of Figs. 6b and c, we established that the north band might be related to the saturated moisture

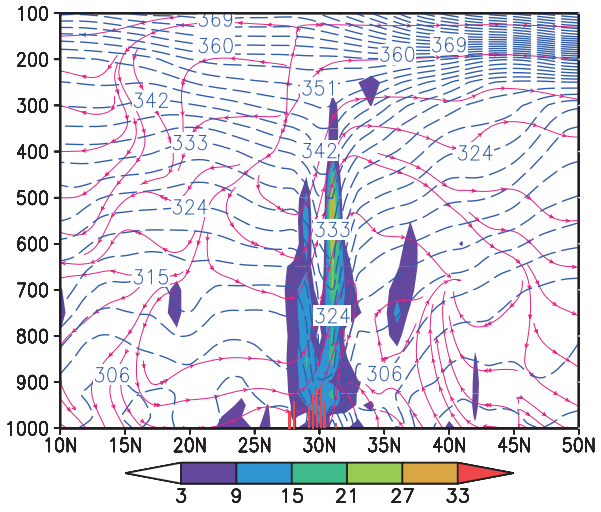

Fig. 9. The meridional vertical sections along 116°E of the non-uniformly saturated frontogenesis function [refer to Eq. (9); shading; units: 10^{-10} K s^{-1} m^{-1}], streamline field (arrowed lines), generalized potential temperature (dashed lines; units: K) and precipitation amount (vertical bar lines) at 0000 UTC 6 July 2003.

column, and the south band might be related to the unsaturated moisture column. Strong updrafts were sandwiched between these two frontal bands. The frontal bands tended to locate slightly on the north side of the corresponding rainbelts, with the saturated frontal band being responsible for the heavy rainband and the unsaturated frontal band being responsible for the light rainband. This picture is consistent with the analyses in Figs. 8a and 3b.

Finally, to analyze the relative contributions to the frontogenesis from the various terms in Eqs. (15) and (17), we plot the time series of the completely saturated and non-uniformly saturated frontogenesis functions and their component terms in Fig. 10. The evolution tendency of the terms showed that although the vertical velocity term is negative near the front (F_2), the large-scale convergence and deformation of the horizontal wind in the frontal zone work together to sustain a positive gradient of θ^* or θ_e against the decrease of the θ^* or θ_e gradient caused by the tilting/twisting effect. The difference between the non-uniformly saturated and completely saturated frontogenesis (compare Figs. 10a and b) is that the non-uniformly saturated frontogenesis function tends to produce a much stronger front in the first 12 hours than the frontogenesis function based on using equivalent potential temperature. After the initial 12 hours, the frontogenesis by the former decreases relatively significantly, while the latter decreases very slightly. But how can we explain this phenomenon? The latter function assumes a saturated atmosphere everywhere, which tends to smooth out the moisture gradient, and therefore reduces the strength of the frontogenesis and the variation tendency of the frontal production. This result is also consistent with previous analyses. Furthermore, the evolution tendency of the non-uniformly saturated frontogenesis function reflects the frontogenesis strength variations (Fig. 10a), which is consistent with the amplification and decay of the weather systems, and the accompanying precipitation evolution (Fig. 10c).

The fit between the values of the non-uniformly saturated frontogenesis function (gridded data) and precipitation amount (corresponding grids) is performed by linear regression ($y = ax + b$, where y is precipitation and x is the frontogenesis function). Figure 10d shows the derived relationship with $a = 8.27$ and $b = 2.45$, and the correlation coefficient equal to 0.86. The relationship in Fig. 10d is used to calculate the intensities of the new generalized frontogenesis function for different rainfall thresholds (Fig. 10d and Table 1). Inversely, the obtained frontogenesis intensity thresholds may be used to predict rainfall with different intensities. For example, if the frontogenesis function is greater than or equal to 11.80 10^{-9} K s^{-1} m^{-1}, precipitation may reach up to heavy-rainstorm level (Table 1). From Fig. 10d, there is greater correlation between the new frontogenesis function and the precipitation as the 24-h rainfall amount is less than 100 mm (below heavy-rainstorm level). At this time, their correlation coefficient can reach up to 0.88. Since the new frontogenesis function may provide an obvious positive correlation with the rainfall to a certain extent, it is helpful for rainfall forecasting in the future. Certainly, further work is required to verify this relationship; however, in the present study, we have taken an important first step, i.e., to derive the new frontogenesis function and attempt to test its correlation with rainfall via two case studies. Thus, we have laid the foundations for further frontogenesis studies in the future.

6. Conclusion

Traditionally, the Lagrangian change in the gradients of θ (or θ_e) is taken as the criterion for frontogenesis in dry (or completely saturated) atmosphere. However, the real atmosphere is neither absolutely dry nor completely saturated, and it is more likely non-uniformly saturated (e.g., near a humidity front). In order to describe a non-uniformly saturated atmosphere, we generalized the potential temperature to include both temperature and moisture effects. With this generalized potential temperature, a generalized frontogenesis function for a non-uniformly saturated moist atmosphere was defined as the Lagrangian change rate of $|\nabla\theta^*|$. The dynamics of various physical processes were analyzed. The non-uniformly saturated frontogenesis function is more appropriate for the real moist atmosphere. In particular, this generalized frontogenesis function improves the traditional frontogenesis function, in which the assumption of either completely dry or completely saturated atmosphere has to be made. Furthermore, the non-uniformly saturated frontogenesis function includes the effect of the moisture gradient, which provides an important dynamic mechanism for the development of fronts in a moist atmosphere.

Diagnostic studies were conducted for two real frontal precipitation cases. It was shown from these diagnoses that the non-uniformly saturated frontogenesis function indeed

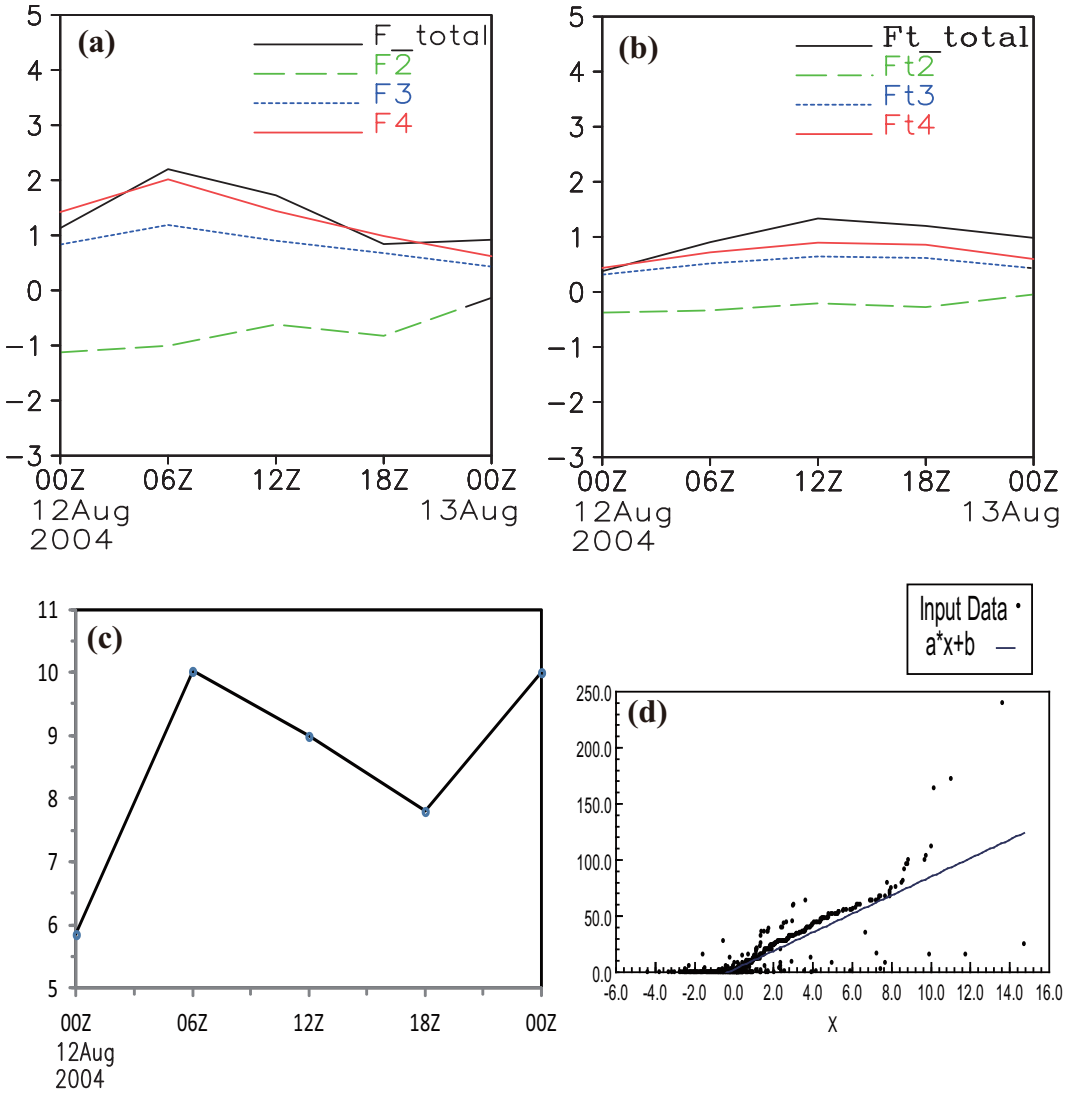

Fig. 10. The curve of area-averaged (36°–42°N, 115°–120°E) terms in the (a) non-uniformly saturated frontogenesis function [refer to Eq. (9); F_total = $F_2 + F_3 + F_4$; F_2: vertical velocity term; F_3: convergence term; F_4: deformation term (units: 10^{-9} K s^{-1} m^{-1})]; (b) traditional frontogenesis function [$F_{t\_total} = F_{t2} + F_{t3} + F_{t4}$; Ft2: vertical velocity term; Ft3: convergence term; Ft4: deformation term (units: 10^{-9} K s^{-1} m^{-1})] at 700 hPa; and (c) precipitation (mm) from 0000 UTC 12 to 0000 UTC 13 August 2004. (d) The fit between the values of the frontogenesis function (gridded data; units: 10^{-9} K s^{-1} m^{-1}) and precipitation amount (mm; corresponding grids) by linear regression ($y = ax + b$, where y is precipitation and x is the frontogenesis function).

Table 1. To calculate the intensities of the frontogenesis function for different rainfall thresholds according to the relationship in Fig. 10d.

24-h rainfall amount (Y, mm)	0.1–10	10–25	25–50	50–100	100–200
Rain level	Drizzle	Rain	Heavy rain	Rainstorm	Heavy rainstorm
Frontogenesis function (X, 10^{-9} K s^{-1} m^{-1})	0.91	2.73	5.75	11.80	23.89

has several advantages. First, the non-uniformly saturated frontogenesis function captured the frontal development due to either the temperature or moisture gradient, or both. Second, the non-uniformly saturated frontogenesis function showed a much stronger and more clear signal in frontal zone than the traditional frontogenesis function. Third, the location, pattern, and strength of the developing front correlate much better with precipitation fields in the analyses using the non-uniformly saturated frontogenesis function than in when using the traditional frontogenesis function. Both the theoretical analyses and diagnostic studies for the real cases showed a promising future for the application of this non-uniformly saturated frontogenesis function.

It is important to note that further description of the generalized potential temperature and the corresponding generalized frontogenesis function is necessary, where the "general-

ized" potential temperature reflects a meaning as follows: θ^* is the continuous function of θ and q in mathematics; therefore, in a certain physical sense approximately represents potential temperature in the dry/moist process as the moisture is less/greater than the critical condensation relative humidity. Furthermore, θ^* can completely regress to the θ and θ_e formula in extreme dry and completely saturated cases. Therefore, although it is only one of the solutions to the problem, the generalized potential temperature, θ^*, seems to possess properties superior to θ_e (e.g., θ^* is a continuous function of θ and q).

Thus, the primary advantage of θ^* over θ or θ_e is handed to and inherited by the non-uniformly saturated frontogenesis function, since it is based on θ^*. Secondly, the application in real cases showed the validity of the non-uniformly saturated frontogenesis function. Furthermore, the frontogenesis strength variations from the evolution tendency of the non-uniformly saturated frontogenesis function also reflects the amplification and decay of weather systems, and the accompanying precipitation evolution.

Acknowledgements. The authors were supported by the National 973 Fundamental Research Program of the Ministry of Science and Technology of China (Grant No. 2013CB430105), the Special Scientific Research Fund of the Meteorological Public Welfare of the Ministry of Sciences and Technology (Grant No. GYHY201406003), the National Natural Sciences Foundation of China (Grant Nos. 41375054, 41375052 and 40805001), and the Opening Foundation of the State Key Laboratory of Severe Weather, Chinese Academy of Meteorological Sciences (Grant Nos. 2012LASW-B02 and 2013LASW-A06).

REFERENCES

Barth, M. C., and D. B. Parsons, 1996: Microphysical processes associated with intense frontal rainbands and the effect of evaporation and melting on frontal dynamics. *J. Atmos. Sci*., **53**, 1596–1586.

Bergeron, T., 1928: *Über die dreidimensional Verknüpfende Wetteranalyse*. Geofys. Publ., **5**, 1–111.

Cohen, R. A., and D. M. Schultz, 2005: Contraction rate and its relationship to frontogenesis, the Lyapunov exponent, fluid trapping, and airstream Boundaries. *Mon. Wea. Rev*., **133**, 1353–1369.

Davies-Jones, R. P., 1982: Observational and theoretical aspects of tornadogenesis. *Intense Atmospheric Vortices*, L. Bengtsson and J. Lighthill, Eds., Springer-Verlag, 175–189.

Davies-Jones, R. P., 1985: Comments on "A kinematic analysis of frontogenesis associated with a nondivergent vortex." *J. Atmos. Sci*., **42**, 2073–2075.

Doswell, C. A., III, 1984: A kinematic analysis of frontogenesis associated with a nondivergent vortex. *J. Atmos. Sci*., **41**, 1242–1248.

Eliassen, A., 1962: On the vertical circulation in frontal zones. *Geofys. Publ.*, **24**(4), 147–160.

Fulton, S., and W. H. Schubert, 1991: Surface frontogenesis in isentropic coordinates. *J. Atmos. Sci.*, **48**, 2534–2541.

Gao, S. T., and J. Cao, 2007: Physical basis of generalized potential temperature and its application to cyclone tracks in nonuniformly saturated atmosphere. *J. Geophys. Res.*, **112**, D18101, doi: 10.1029/2007JD008701.

Gao, S. T., X. R. Wang, and Y. S. Zhou, 2004: Generation of generalized moist potential vorticity in a frictionless and moist adiabatic flow. *Geophys. Res. Lett.*, **31**, L12113, 1–4.

Gao, S. T., Y. Zhou, T. Lei, and J. H. Sun, 2005: Analyses of hot and humid weather in Beijing city in summer and its dynamical identification. *Science in China (D)*, **48**, 128–137.

Gao, S. T., S. Yang, and B. Chen, 2010: Diagnostic analyses of dry intrusion and nonuniformly saturated instability during a rainfall event. *J. Geophys. Res.*, **115**, D02102, doi: 10.1029/2009JD012467.

Hoskins, B. J., and F. P. Bretherton, 1972: Atmospheric frontogenesis models: Mathematical formulation and Solution. *J. Atmos, Sci.*, **29**, 11–37.

Keyser, D., M. J. Pecnick, and M. A. Shapiro, 1986: Diagnosis of the role of vertical deformation in a two-dimensional primitive equation model of upper-level frontogenesis. *J. Atmos. Sci.*, **43**, 839–850.

Li, N., L. K. Ran, Y. S. Zhou, and S. T. Gao, 2013: Diagnosis of the frontogenesis and slantwise vorticity development caused by the deformation in the Beijing "7. 21" torrential rainfall event. *Acta Meteorologica Sinica*, **71**, 593–605. (in Chinese)

Mason, B. J., 1971: *The Physics of Clouds.* 2nd Ed. Oxford University Press, 671pp.

Miller, J. E., 1948: On the concept of frontogenesis. *J. Meteor.*, **5**, 169–171.

Newton, C. W., 1954: Frontogenesis and frontolysis as a three-dimensional process. *J. Atmos. Sci.*, **11**, 449–461.

Ninomiya, K., 1984: Characteristics of Baiu front as a predominant subtropical front in the summer northern hemisphere. *J. Meteor. Soc. Japan*, **62**, 880–893.

Ninomiya, K., 2000: Large-and meso-scale characteristics of Meiyu/Baiu front associated with intense rainfalls in 1–10 July 1991. *J. Meteor. Soc. Japan*, **78**, 141–157.

Petterssen, S., 1936: Contribution to the theory of frontogenesis. *Geofys. Publ.*, **11**(6), 1–27.

Petterssen, S., 1956: *Weather Analysis and Forecasting.* Vol. 1, *Motion and Motion Systems*, 2nd ed. McGraw-Hill, 428 pp.

Ran, L. K., and Y. L. Chu, 2007: Diagnosis of the slantwise development of isentropic and moist isentropic surfaces. *Chinese J. Atmos. Sci.*, **31**, 655–665. (in Chinese)

Ran, L. K., W. X. Yang, and Y. L. Chu, 2010: Diagnosis of dynamic process over rainband of landfall typhoon. *Chinese Physics* (*B*), **19**, doi: 10.1088/1674-1056/19/7/079201.

Reed, R. J., 1955: A study of a characteristic type of upper-level frontogenesis. *J. Atmos. Sci*., **12**, 226–237.

Sawyer, J. S., 1956: The vertical circulation at meteorological fronts and its relation to frontogenesis. *Proc. Roy. Soc. London* (*A*), **234**, 346–362.

Wang, C. W., R., Wu, and Y. Wang, 2002: Interaction of diabatic frontogenesis and moisture processed in cold-frontal rain-band. *Adv. Atmos. Sci*., **19**, 544–561.

Wu, R. S., and Coauthors, 2004. *Dynamics of Front and Mesoscale Disturbances*. China Meteorological Press, Beijing, 6–57. (in Chinese)

Wu, X. D., L. K. Ran, and Y. L. Chu, 2011: Diagnosis of a moist thermodynamic advection parameter in heavy-rainfall events. *Adv. Atmos. Sci.*, **28**, 957–972, doi: 10.1007/s00376-009-9057-8.

Yang, S., and S. T. Gao, 2006: Modified Richardson number in non-uniform saturated moist flow. *Chinese Physics Letters*,

23, 3003–3006.

Yang, S., and D. H. Wang, 2009: Diagnostic analyses of the modified convective vorticity vector in non-uniformly saturated moist flow. *Atmos. Oceanic Sci. Lett.*, **2**, 142–147.

Yang, S., S. T. Gao, and D. H. Wang, 2007: Diagnostic analyses of the ageostrophic Q vector in the non-uniformly saturated, frictionless, and moist adiabatic flow. *J. Geophys. Res.*, **112**, D09114, doi: 10.1029/2006JD008142.

Yang, S., X. P. Cui, and L. K. Ran, 2009: Analyses of dry intrusion and instability during a heavy rainfall event that occurred in Northern China. *Atmos. Oceanic Sci. Lett.*, **2**, 108–112.

Yu, X., E. Richard, and R. Rosset. 1995: A numerical investigation of the impact of latent heating upon the structure of active cold fronts. *Acta Meteorologica Sinica*, **53**, 319–327.

Zhao, Q. Y., and F. H. Carr, 1997: A prognostic cloud scheme for operational NWP models. *Mon. Wea. Rev.*, **125**, 1931–1953.